Shaping Perovskites: In-Situ Crystallisation Mechanism of Rapid-Thermally Annealed, Pre-Patterned Perovskite Films

Antonio Günzler,[†] Esteban Bermúdez-Ureña,[†] Loreta A. Muscarella,[‡] Mario Ochoa,[¶] Efraín Ochoa-Martínez,[†] Bruno Ehrler,[‡] Michael Saliba,[*,§] and Ullrich Steiner[*,†]

[†]Adolphe Merkle Institute, University of Fribourg, Chemin des Verdiers 4, 1700 Fribourg, Switzerland

[‡]Center for Nanophotonics, AMOLF, Science Park 104, 1098 XG Amsterdam, The Netherlands

[¶]Laboratory for thin-films and Photovoltaics, Empa-Swiss Federal Laboratories for Materials Science and Technology, Ueberlandstrasse 129, 8600, Duebendorf, Switzerland

[§]Institute for Photovoltaics (ipv), University of Stuttgart, Pfaffenwaldring 47, Stuttgart D-70569 Germany

E-mail: michael.saliba@ipv.uni-stuttgart.de; ullrich.steiner@unifr.ch

Abstract

Understanding and controlling the crystallisation of organic-inorganic perovskite materials is important for their function in optoelectronic applications. This control is particularly delicate in scalable single-step thermal annealing methods. In this work, the crystallisation mechanisms of flash infrared annealed (FIRA) perovskite films,

1

grown on substrates with lithographically patterned Au nucleation seeds, are investigated. The patterning enables the *in-situ* observation to study the crystallisation kinetics and precise control of the perovskite nucleation and domain growth, while retaining the characteristic polycrystalline micro-morphology with larger crystallites at the boundaries of the crystal domains, as shown by electron backscattering diffraction. Time resolved photoluminescence measurements reveal longer charge carrier lifetimes in regions with large crystallites on the domain boundaries, relative to the domain interior. By increasing the nucleation site density, the proportion of larger crystallites is increased. This study shows that the combination of rapid thermal annealing with nucleation control is a promising approach to improve perovskite crystallinity and thereby ultimately the performance of optoelectronic devices.

1 Introduction

Perovskite solar cells (PSCs) have seen a rapid increase in power conversion efficiency (PCE) over the past decade of research to now 25.5%, approaching established technologies.[1–4] Reaching ever closer to the theoretical Shockley-Queisser limit at PCEs of ~33%,[5,6] increasing focus has shifted to the long term stability (i.e. device lifetime) of PSCs and possible strategies for upscaling from a lab- to industry-scale production.[7] The commonly-employed antisolvent method, where an antisolvent is dripped onto the liquid precursor, however, is challenging to scale up at potentially high economic and ecological costs.[8]

Drawing inspiration from the market leading silicon based photovoltaics (PV), large single-crystal active layers are one proposed ideal.[9] However, challenges remain related to the incorporation of perovskite single crystals into the overall device architecture and ensuring optimal contacts to the electron/hole selective layers to reach polycrystalline PCEs,[10] and the fabrication of single crystal perovskite devices is often still complex.[11,12] Whereas high-end fabrication methods, for instance metal organic chemical vapour deposition or hybrid vapor phase epitaxy, are bringing other crystalline thin film PV technologies close to PCEs

of 30%,[1,13,14] new strategies are required to push for such efficiencies in PSCs.

Therefore, in order to maintain the advantages of solution-based processing and controlling the film crystallinity, a major challenge is to fundamentally understand and control the crystallisation processes when the perovskite active layer is formed from its precursors, most commonly from a solution or vapor.[7,15–17] While perovskites show a remarkable tolerance to defects,[18] it has also been observed that the boundaries of individual crystallites (often referred to as *grains*) are frequently the origin of degradation processes.[19] Strategies to mitigate performance losses include precursor additives to control morphology, passivation with polymeric nanolayers, and stoichiometric tuning of the perovskite, which all come with increased complexity and drawbacks.[20–24] A comprehensive understanding of perovskite film growth mechanisms is not only critical for the benefit of solar cell applications, but also for other emerging perovskite based light technologies such as light-emitting devices, detectors, lasers and sensors, for many of which patterning of the perovskite material has gained considerable attention.[25–27]

In this work, we employ a model system that spatially predetermines nucleation sites for perovskite films annealed by the flash infrared annealing (FIRA) method.[28,29] This approach is also suitable for other antisolvent-free thermal annealing methods compatible with large-scale device production (e.g. meniscus-assisted printing),[30] where the crystallisation process is exclusively driven by thermal evaporation of the solvents.[31,32] Methylammonium lead tri-iodide ($MAPbI_3$), one of the most studied perovskite compositions, was selected here to demonstrate the facile crystallisation control. The FIRA method, yielding highly efficient $MAPbI_3$ PSCs, was used to anneal $MAPbI_3$ films on substrates with photolithographically patterned arrays of Au nucleation seeds.[33] The resulting morphologies are then characterised using electron backscattering diffraction (EBSD) and time resolved photoluminescence (TRPL) mapping. Other perovskite compositions were then investigated in the same manner to further elucidate the crystallisation dynamics.

To gain further insight into the morphology evolution of perovskite films, we combine

the deterministic nucleation-site patterning with an in-situ observation method by optical microscopy.[34] The patterned nucleation seeds enable us to identify the location of nucleation *a priori* in order to investigate the nucleation and crystal growth dynamics of the perovskite films. We also show that the method of pre-patterned nucleation sites can be generalised to other commonly-used perovskite compositions.

2   Results & Discussion

2.1   Pre-patterned FIRA-annealed Perovskite Films

FIRA is a rapid antisolvent-free annealing method that produces perovskite films with distinct polycrystalline morphologies that exhibit large polycrystalline domains. Each of these domains forms from a nucleation site and they produce a weighted Voronoi tessellation according to the geometry of the nucleation sites.[28,35] The weighting in the Voronoi tessellation results from a temporal variance of the spontaneous supersaturation-driven nucleation, where spontaneous nucleation can be both homogeneous nucleation from the precursor solution and heterogeneous nucleation caused by contaminants, the substrate surface or the liquid-gas interface.[36] Each domain has a characteristic intrinsic morphology consisting of small individual crystallites in the centre close to the nucleation site and larger crystallites close to the boundaries of the domains.[37] The diameters of the domains are typically in the $100 - 300\,\mu\mathrm{m}$ range.[28]

The domain nucleation sites can be spatially predetermined by patterning silicon and tin doped indium oxide (ITO) coated glass substrates with hexagonal arrays of Au seeds, as demonstrated by Geske *et al.*[33] They hypothesise a lowering interfacial energy at the Au surface caused by a catalytic effect of the Au to give rise to the nucleation effect. The details of this nucleation effect are, however, currently unclear.

In the present study, the reported patterning method is combined with the FIRA deposition and annealing protocol for the manufacture of pre-patterned $MAPbI_3$ and methylam-

monium lead tri-bromide (MAPbBr$_3$) films, as previously established by Sánchez *et al.*,[29] that has demonstrated competitive device performances. The pre-patterned perovskite films of this study, therefore, resemble the nucleation and crystallisation kinetics under deposition parameters relevant to rapid-thermally annealed high-performance PSCs.
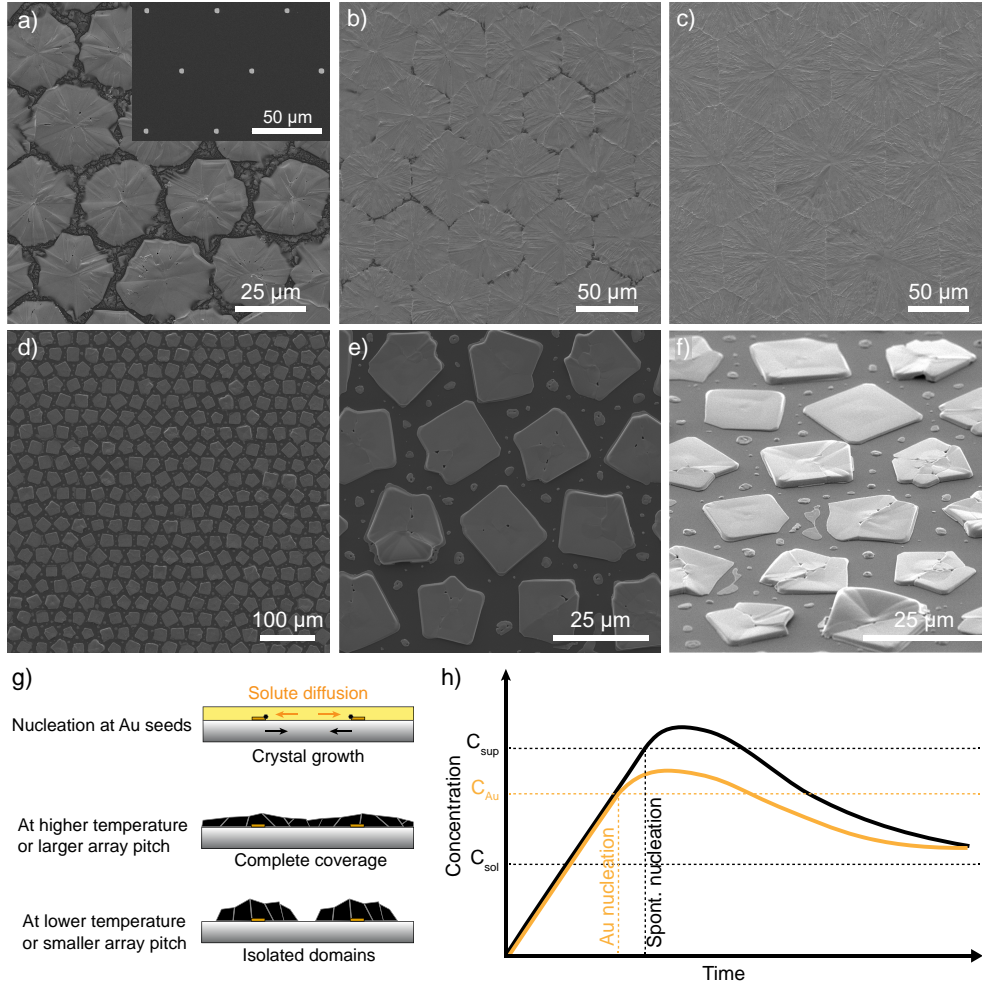

Figure 1: FIRA-annealed MAPbI$_3$ samples on Au seed patterned Si substrates. Au seeds function as predetermined nucleation sites patterned as a hexagonal lattice with varying pitches of (a) 30 µm (inset: Au-patterned Si substrate), (b) 60, and (c) 90 µm. The inset in (a) shows the patterned substrate. (d–f) SEM images of FIRA-MAPbBr$_3$ on Au-patterned Si substrate with a 25 µm pitch: (d) top view overview, (e) close-up, and (f) tilted at 45°. g) Schematic illustration of nucleation, crystal growth, and solute diffusion for different parameters. (h) LaMer curve for the spontaneous and Au seeded nucleation, indicating the lowered concentration threshold for the latter.

Figure 1a-c and d-f show FIRA annealed MAPbI$_3$ and MAPbBr$_3$ films, respectively, for various pitch sizes of predetermined nucleation sites (Au patches on Si substrate shown

in the inset in Figure 1a). By varying the distance between the Au seeds, the density of the nucleation sites, and thus the shape and size of the domain can be controlled. Si and ITO coated glass substrates were pre-patterned to obtain compact perovskite films with hexagonal domains of tunable diameters in the $30 - 100\,\mu m$ range. The geometric regularity of the domains within the patterns shows that predetermined nucleation has very little temporal variance, i.e. all nuclei form almost simultaneously, producing an unweighted Voronoi tessellation, whenever sufficient precursor material is available for the domains to grow until they meet. At spacings larger than $100\,\mu m$, spontaneous nucleation was observed, forming perovskite domains between the Au seeded domains. At patch distances of $30\,\mu m$ and below, the diffusion of precursor molecules toward the crystallisation front leads to depleted areas between the isolated domains, as shown in Figure 1a,d-f. Note, however, that despite the precursor depletion at a seed pitch of $30\,\mu m$ in Figure 1a, some of the domains appear to have hexagonal shapes. This is due to a surface tension and convection effect in the precursor solution during thermal annealing, which is further discussed below.

The depletion results from the vicinity of seeded nucleation sites, as a higher density of growing crystal domains compete for precursor molecules. Since the annealing conditions with FIRA were kept identical, the different film morphologies solely depend on the pitch of the patterned hexagonal Au seed arrays. Because the nucleation and crystal growth locally remove solutes from the solution, a concentration gradient is created with a lower solute concentration at the crystal growth front than in the bulk solution. Precursor molecules, therefore, diffuse toward the growing domains, which can lead to depleted areas for sufficiently small pitch sizes or low annealing temperatures, where thermal solvent evaporation is not outpacing solute diffusion (see schematic in Figure 1g). At higher temperatures, crystal growth parallel to the substrate outpaces solute diffusion due to fast solvent evaporation. At the same time, increasing the array pitch, i.e. the distance between Au seeds, results in a lower density of patterned nucleation sites competing for solutes, and thus no complete solute depletion between the domains. For MAPbBr$_3$, the depletion effect is more prominent

than for MAPbI$_3$, leading to entirely isolated domains that consist of only a few individual single crystals, even at array pitch distances of 50 μm, resulting in isolated platelets and partially connected domains (Figure S1). The cubic crystal lattice of MAPbBr$_3$ probably enables the growth of oriented cuboid single crystals with one facet aligned to the substrate surface.[33,38]

A simplified classical nucleation and crystal growth model is described by the so-called LaMer curve,[39] relating crystallisation mechanisms to the solution concentration, which has also been applied to illustrate crystallisation kinetics in perovskite films.[28,40] The LaMer curve shows the concentration as a function of time, increasing due to solvent evaporation until the supersaturation limit for nucleation is reached. Once solutes are removed from the solution due to crystallisation the concentration decreases as a result. The absence of spontaneously nucleated domains, according to the LaMer model, between the Au seeded domains in all pre-patterned films indicates that the solution film in the pre-patterned regions never reaches the supersaturation threshold required for spontaneous nucleation, C_{sup}, as indicated in the modified LaMer curve in Figure 1h. Instead, nucleation at the Au seeds occurs at lower concentration, C_{Au}. Although continued heating leads to sustained solvent evaporation the simultaneous crystallisation of the precursor molecules counteracts the increase in concentration, such that C_{sup} is never reached before Au seeded domain formation and crystallisation are complete. This is discussed in more depth below.

Since standard SEM imaging is limited in identifying the crystalline nature of the domains, electron backscattering diffraction (EBSD) mapping was used to compare the micromorphology of pre-patterned MAPbI$_3$ domains with spontaneously nucleated films, by determining the spatial distribution of crystallites within the domains, their dimensions and orientations (Figure 2a-d). Figure 2a shows the overlap of the image quality (brightness, IQ) with the Inverse Pole Figure (color, IPF) representing the signal intensity and the crystal orientation obtained from fitting the Kikuchi lines (Figure 2c) to each pixel of the scanned area perpendicular to the substrate, respectively. Perpendicular to the substrate (z-axis),
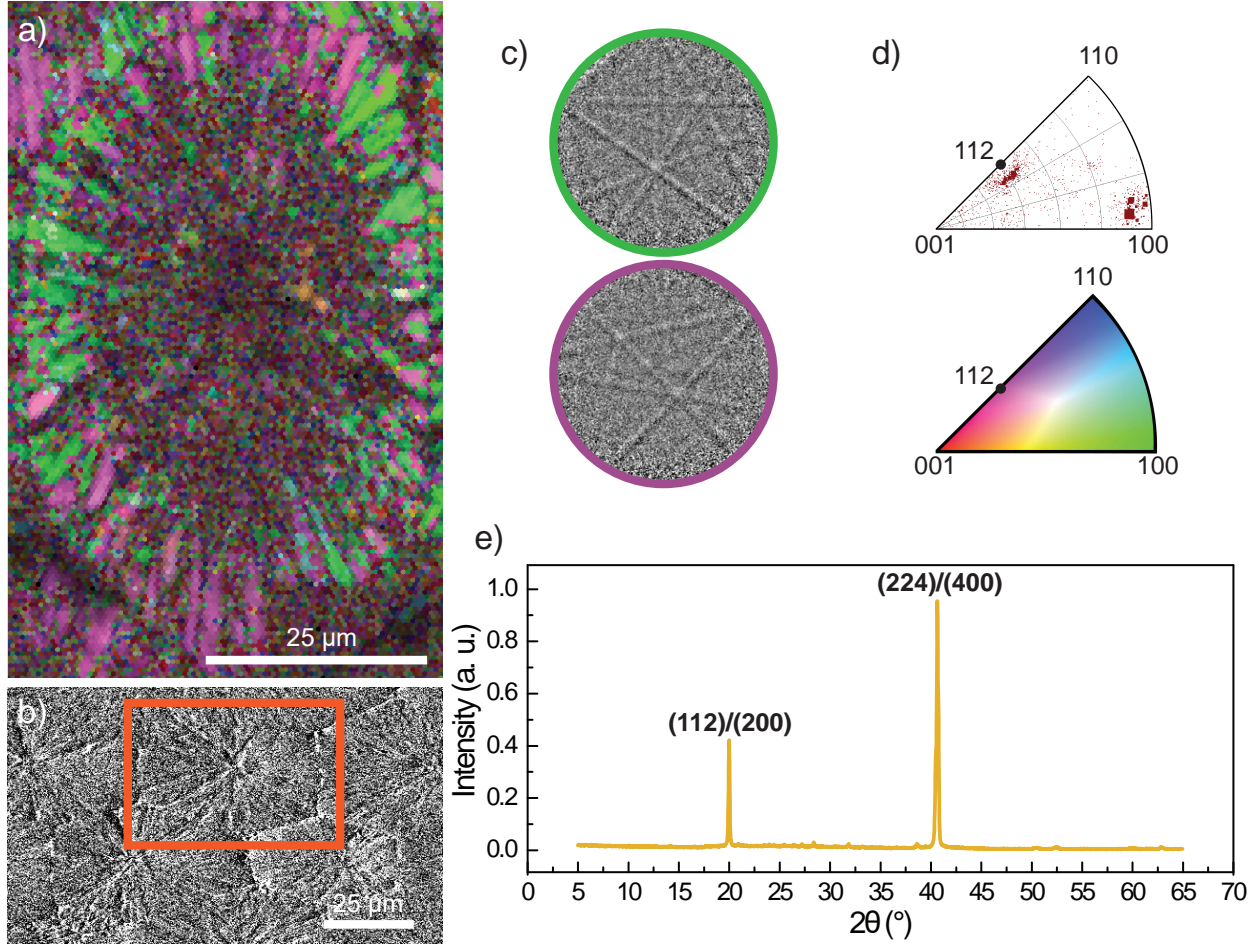
Figure 2: Micro-morphology of rapid-thermally annealed MAPbI$_3$ crystal domains. (a) EBSD map indicating the crystallographic orientations in z-direction. (b) SEM image indicating the measured area within the pattern for the EBSD mapping. (c) Kikuchi patterns identifying the two dominant crystallographic orientations. (d) Distribution of crystallographic orientations over the measured area. (e) XRD data for a pre-patterned MAPbI$_3$ film on an ITO-coated glass substrate.

EBSD reveals domains preferentially oriented along the (112) and (100) orientations as confirmed by the X-ray diffraction (XRD) data shown in Figure 2e. The XRD data is indicative of the characteristic preferential crystal orientations (112) and (100), showing peaks at 20° corresponding to the (112) and (200) reflections and at 40.5° corresponding to the (224) and (400) reflections that are also observed in non-patterned FIRA-annealed MAPbI$_3$ perovskite films[37] and in orientationally pure crystalline films grown in a thermal gradient parallel to the substrate.[41,42] EBSD mapping allows to distinguish individual crystallites by

determining their in- and out-of-plane crystal orientations, showing that crystallites close to the domain boundaries tend to be larger than in the interior of the domains. This polycrystalline morphology of the domains with increasing crystallite sizes toward the domain boundaries, revealed by the EBSD measurements, indicates that a secondary heterogeneous nucleation process, originating from the crystal growth fronts at the substrate surface or the liquid-gas interface, gives rise to the characteristic crystal morphology of the domains. For completeness, the crystallographic orientations along x- and y-directions are shown in Figure S2.

If the crystallite size depended only on their absolute distance to a nucleation site, increasing the nucleation site density would yield smaller domains, and thus a smaller average crystallite size. However, the opposite effect is observed, where the larger boundary crystallites appear merely closer to the nucleation sites, indicating that the characteristic polycrystalline morphology is independent of the final domain size. Therefore, by increasing the nucleation density, the crystallite size distribution of the entire film is biased toward larger crystallite sizes.

The photoluminescence (PL) lifetime in perovskite films depends on the size of crystallites within a polycrystalline assembly.[43] TRPL mapping was used to investigate whether the crystalline morphology within the domains correlates with optoelectronic properties. In these experiments, the spatially resolved PL intensity and charge carrier lifetime (τ) within a domain of pre-patterned perovskite films were compared to an unpatterned reference area without Au seeds (Figure 3). Both areas show a strong correlation of crystalline micro-morphology with the PL intensity (Figure 3a,b) and τ-maps (Figure 3c,d) indicating that micro-morphology determines the luminescence and charge carrier dynamics. In the interior of the domains (position A in the PL maps), where the EBSD measurements show small crystallites, the lifetime is approximately two times shorter than in larger crystallites near the domain boundaries (position B in the PL maps). Representative PL transients of these regions are illustrated in Figure 3e,f for pre-patterned and reference areas, respectively.
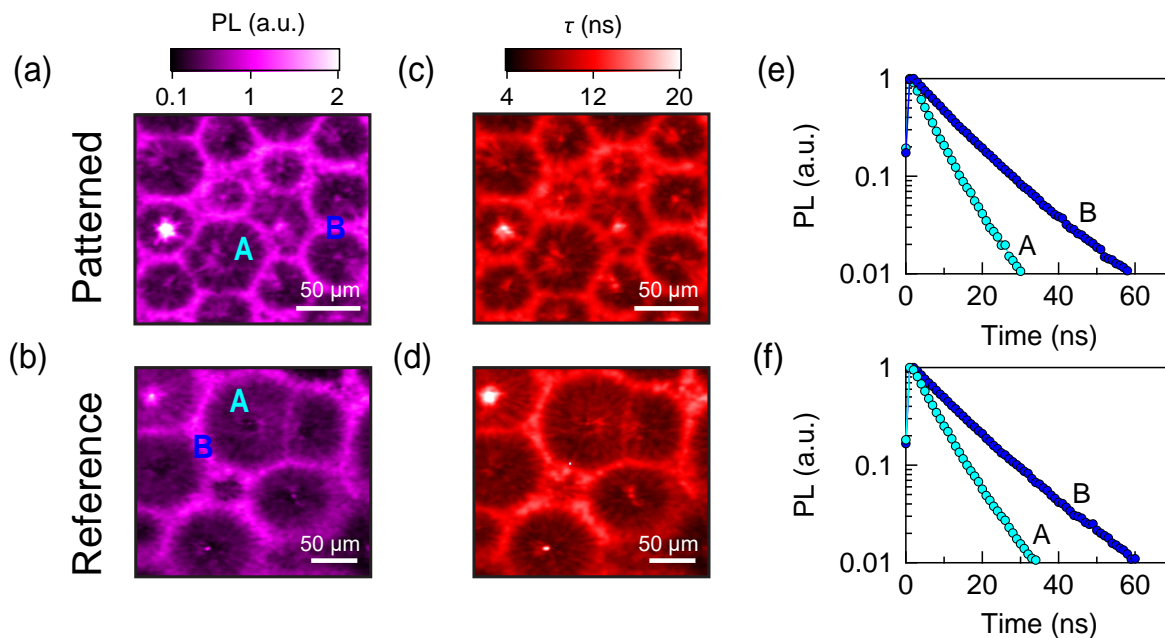
Figure 3: Time-integrated PL and τ maps of pre-patterned (a–b) and reference (c–d) rapid-thermally annealed MAPbI$_3$ films. Normalised TRPL decays at two different locations (A: domain interior & B: near domain boundary) indicated in the lifetime maps for both pre-patterned (e) and reference area (f). The pre-patterned domains exhibit larger area fill fraction of near-boundary crystallites with higher carrier lifetime as compared to crystallites on the domain interior. The TRPL decays correspond to the average signal of 100 pixels.

Both patterned and reference areas exhibit very similar decays in each region of $\sim$5 ns in the interior (position A) of a pre-patterned domain (6 ns for the reference) and $\sim$11 ns near the boundaries (position B, 12 ns for the reference). Hence, we conclude that the characteristic micro-morphology is preserved in Au seeded pre-patterned domains and there is no evident modification of the PL characteristics by increasing the nucleation site density as compared to the reference area. By retaining this distribution of crystallite sizes within each domain, increasing the nucleation site density by patterning increases the proportion of large near-boundary crystallites that contribute to overall longer PL lifetime of the entire perovskite film.

At the same time, seeding also has an effect on the morphology of the centres of the domains, i.e. close to the nucleation site (Figure S3). The TRPL signal from the domain centres includes, however, a non-quantifiable contribution from the Au seed, making a TRPL

comparison of the domain centres difficult. Unfortunately, due to the difference in roughness of the film between the centre and the rest of the domain, also EBSD mapping was not able to resolve the crystallite dimensions at the domain centres. Figures S9 and S10 show exemplary AFM and cross-sectional SEM images, respectively. Note, however, that the topography and thickness of the films vary significantly with all the experimental parameters, such as Au array pitch, perovskite composition and annealing time, temperature and method.

Note that the presence of the Au seeds after crystallisation could make this architecture impractical for the use in solar cell devices, due to the introduction of trap states and recombination sites, as well as degradation processes due to Au migration.[44,45] The deterministic nucleation effect of other metals (e.g., Pt and Cu) was also tested, but their effect was not as consistent as that of Au, while a non-metallic material such as SiO_2 did not show a nucleating effect at all (Figure S4). A material that is chemically and optoelectronically inert after crystallisation but provides a similar nucleation-catalytic effect would be an interesting candidate material for future integration into devices.

2.2 In-situ Observation of Nucleation and Crystallisation

To further study the dynamic formation kinetics of the domain morphologies on patterned and unpatterned substrates, we observed the nucleation and crystallisation processes *in-situ* under an optical microscope[34] using a heating stage to approximate the thermally induced solvent evaporation that drives the film crystallisation in the FIRA experiments. While FIRA is able to reach much higher peak temperatures and, therefore, shorter annealing times, we show that the hotplate annealing achieves the same characteristic film morphology. Figure 4a-e shows a sequence of snapshots corresponding to the different stages of nucleation and growth of $MAPbI_3$ perovskite domains. The substrate was heated to a constant temperature under the optical microscope followed by drop-casting $2\,\mu L$ of a precursor solution onto the substrate. In each experiment, visible nucleation occurred simultaneously at all seed patches (within $0.14\,s$). The growth rate, as defined by the area increase of the domains,

was uniform, leading to regular hexagonal arrays of perovskite domains. Figure 4f-j shows a similar *in-situ* experiment, in which the precursor solution was spin-cast onto the substrate, similar to the FIRA fabrication protocol. In these spin-coated films, a polycrystalline micro-morphology similar to that in FIRA films was obtained. (SEM image in Figure S5.) The thinner spin-cast solution film leads to an initially growing domain that reaches the liquid-air interface, inducing a secondary heterogeneous nucleation on the surface of the solution film, such that the domain grows in an alternating cascade of nucleation- and diffusion-driven growth.
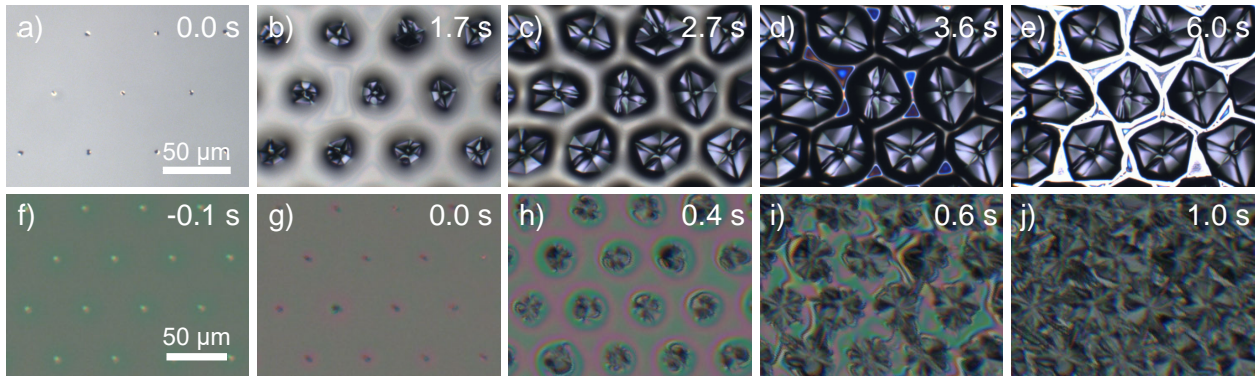

Figure 4: In-situ observation of nucleation and crystallisation of MAPbI$_3$ films on an Au-patterned Si substrate heated to a constant temperature of 110 °C: (a–e) drop-cast, (f–j) spin-coated for 10 s at 4000 rpm (as for FIRA) and subsequently annealed at 110 °C during *in-situ* observation.

The observations in the *in-situ* experiments confirm the regularity of the domain patterns observed in the FIRA samples (Figure 1a-f). The nucleation at the Au seeds was simultaneous and the crystallisation growth rate from each Au patch (Figure 1h) was uniform, which leads to nearly perfect honeycomb patterns, seeded by the hexagonal Au lattice. In this seeded nucleation process, the saturation threshold for nucleation is sufficiently lowered, such that no domains originating from spontaneous nucleation were observed in the area occupied by the Au seed pattern.

Compared to spontaneously nucleated FIRA domains, the precursor solution adjacent to the nucleated crystal growth front is, therefore, not close to the supersaturation limit, C_{sup} (Figure 1h), confirming the interpretation of the FIRA experiments (Figure 1a-f). Hence,

secondary heterogeneous nucleation on the surface of the growing crystals is less frequent, resulting in fewer interruptions of growth of individual crystallites. This yields larger crystallites at the domain centres, relative to the domain interior, as shown in Figure S3.

In the case of spontaneous nucleation, the crystallisation is overall faster because the solution is close to C_{sup} in the entire film, hence, also adjacent to a growing crystal domain. This on the one hand leads to rapid crystal nucleation and growth, outpacing solute diffusion to the crystallites. While providing good substrate coverage, this on the other hand results in small individual crystallites that form in a series of interrupted nucleation and growth processes.
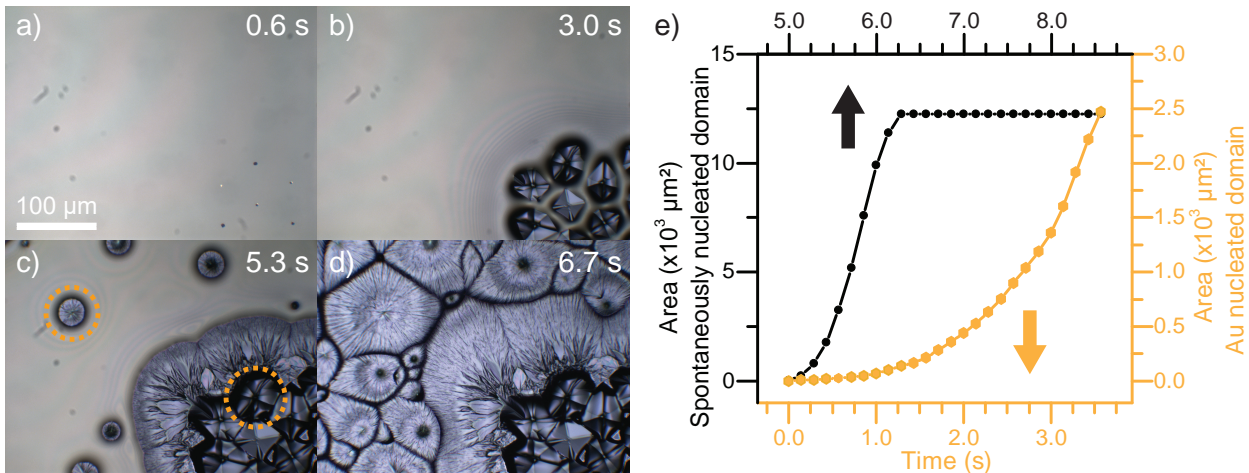

Figure 5: (a–d) MAPbI$_3$ crystallising on a patterned Si substrate heated to $110\,°\text{C}$ from a drop cast precursor solution. The images view a corner of a patterned array and a substrate region without nucleation seeds. (e) Measured area of an Au seed-nucleated and a spontaneously nucleated domain with respect to the first frame in which they were visible [indicated by dotted circles in (c)].

The interplay of solute diffusion and crystal growth rate also affects the substrate coverage in the Au nucleated case (see Figure 1g). Lowering the saturation threshold of nucleation reduces the initial rate of crystal growth, and thus the diffusion of solutes is relatively faster, leading to larger crystallites but also a higher degree of material accumulation close to the nucleation site (i.e. locally thicker perovskite domains). Figure 5a-d show a direct comparison of Au seeded and spontaneous nucleation and subsequent diffusion driven crystal growth of

the domains in the same film. The time offset between the nucleation types correlates to the offset in supersaturation thresholds, C_{sup} and C_{Au}, as the solvent evaporates over time (Figure 1h). The images also show that the absence of spontaneous nucleation in the pre-patterned areas, as discussed above, does not only arise from precursor depletion near the growing seeded crystals but also from the mentioned time offset due to different critical concentrations for the respective nucleation types. In the region beyond the Au seeded pattern, spontaneous nucleation only occurs once the solution reaches C_{sup}, when the Au-seeded domains have already reached their maximum extent.

The difference in crystal growth rate is shown in Figure 5e. Both for seeded and spontaneous nucleation, the final size of the domains is determined by adjacently grown domains, i.e. by the Voronoi tessellation of all nucleation sites. Spontaneous nucleation occurs for a more supersaturated solution compared to seeded nucleation and their rapid growth yields a different micro-morphology.

The Au seeded nucleation leads to diffusion driven domain growth, whereas the spontaneously nucleated domain growth is characterised by a more rapid interplay between diffusion driven crystal growth and heterogeneous secondary nucleation of the highly supersaturated precursor solution near the surface of the crystal growth front. This growth mechanism leads to a star like polycrystalline micro-morphology similar to the morphology in FIRA annealed MAPbI$_3$ perovskite films.[28,37]

Seeding the nucleation of perovskite domains at low solution concentrations during solvent evaporation, thus, enables an improved control over the polycrystalline morphology in single-step rapid-thermally annealed perovskite films. The effect of lowering the saturation threshold can. however. lead to disconnected domains due to material depletion between the growing domains, which is governed by an interplay of the crystal growth rate relative to the diffusion of the solutes and the distance between nucleation seeds. Well-defined disconnected perovskite domains may on the one hand be useful for some applications,[46] particularly in the case of the cubic MAPbBr$_3$ that forms faceted isolated domains (Figure 1d-f). If, on

the other hand a uniform substrate coverage is desired, the nucleation site density and the annealing temperature have to be appropriately adjusted.
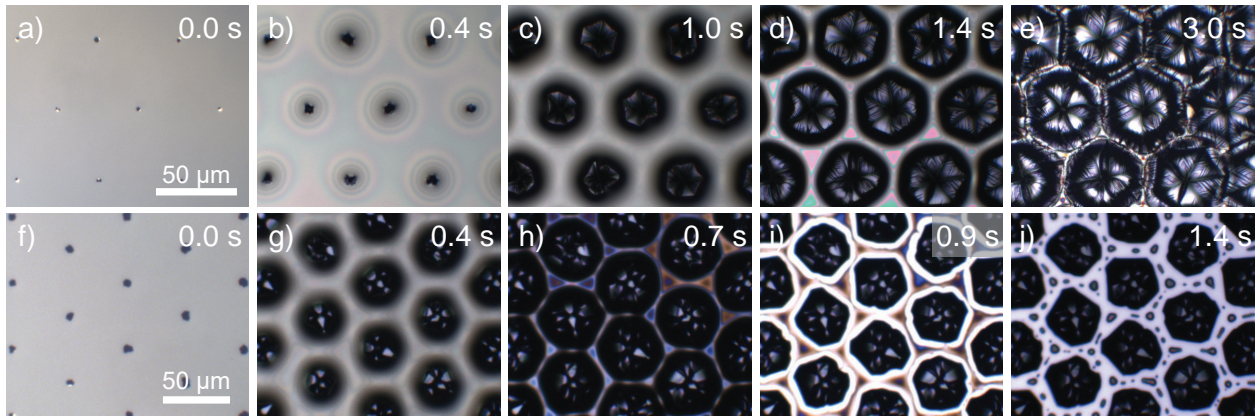

Figure 6: (a–e) Triple cation perovskite, $Cs_{0.05}(MA_{0.17}FA_{0.83})_{0.95}Pb(I_{0.83}Br_{0.17})_3$, nucleating and crystallising on an Au patterned Si substrate from a drop-cast precursor solution on a hotplate set to a constant temperature of $110\,°C$. (f–j) $MAPbI_3$ perovskite nucleation and growth from a pure DMF-based precursor solution, drop cast onto an Au patterned Si substrate at $110\,°C$.

Importantly, Au seed patterning also works for a range of perovskite compositions such as the high-bandgap $MAPbBr_3$ (Figure 1d-f), the widely used triple cation $Cs_{0.05}(MA_{0.17}FA_{0.83})_{0.95}Pb(I_{0.83}Br_{0.17})_3$ (Figure 6a-e), and the MA-free $Cs_{0.15}FA_{0.85}PbI_3$ (Figure S6).

In particular, the triple cation and the dimethylformamide (DMF) based $MAPbI_3$ offer further insight into the morphology formation in single-step rapid-thermally annealed perovskite films. At low growth speeds parallel to the substrate, pattern formation is aided by surface tension and convection effects, also observed in domain formation in meniscus coating methods of perovskites.[47] The thin-film interference visible in the optical microscopy images in Figures 4 and 6 between the growing domains shows that the thickness of the solution film varies between the growing domains. This effect is strongest in the pure-DMF based $MAPbI_3$ depicted in Figure 6f-j, where dewetting of the solution film produces a secondary and tertiary lattice of small domains. This ripple effect is due to a complex interplay of solution flow, solute diffusion, the solvent evaporation and the crystal growth.[48,49]

This effect depends strongly on the crystal growth kinetics and thus on both the per-

ovskite composition and the solvent mixture. The pure-DMF based MAPbI$_3$ precursor solution lacks the crystallisation retardation afforded by dimethylsulfoxide (DMSO) and the material accumulates more strongly close to the nucleation sites.

In meniscus-assisted solution printing of perovskites, He *et al.* found an initially high crystal growth rate after nucleation, causing the domains to grow quadratically with time (corresponding to linear radial growth) and a second slower phase with a linear area growth caused by an overlap of the solute diffusion areas of several growing crystals.[30] Figure 5e shows an initial high crystal growth rate after nucleation in the *in-situ* observation, due to continued solvent evaporation. The growth rate reaches an inflection point when the diffusion areas of adjacently growing domains overlap slowing down crystal growth until the domains meet, forming their mutual boundaries. The change in growth rate corresponds to the observation of varying crystallite sizes within the domains regardless of domain size. Thus, the crystallite size within the micro-morphology of the domains is determined by the crystal growth rate rather than the absolute distance to the nucleation site.

DMSO plays an important role in affecting the crystal growth rate. It strongly coordinates with PbI$_6$ molecules, forming a metastable intermediate phase in the crystallisation process of MAPbI$_3$, thus retarding the crystallisation process.[50–52] To understand its effect in the crystallisation process, we repeated the *in-situ* experiment with a precursor solution of MAPbI$_3$ in pure DMF. Figure 6b shows that, without the DMSO mediated metastable phase, crystal growth parallel to the substrate is slowed down, suggesting that the intermediate phase is critical in achieving uniform compact films.

Moreover, at equal temperatures, the $Cs_{0.05}(MA_{0.17}FA_{0.83})_{0.95}Pb(I_{0.83}Br_{0.17})_3$ composition achieves more uniform substrate coverage compared to MAPbI$_3$ (see Figure 6a), suggesting that the high efficiency and stability of this perovskite composition do not only arise from its chemical composition, but that the heterogeneity in its components prevents a highly ordered faceted crystal growth immediately after nucleation.

Spatial heterogeneity in triple-cation perovskite films observed by Bercegol *et al.* suggests

that the role of Cs doping may be the facilitation of favourable morphology evolution during crystallisation rather than optoelectronic effects due to its presence in the crystallised perovskite film.[53,54] Figure S7 shows that XRD measurement of a triple cation perovskite film annealed with FIRA is in good agreement with a reference film prepared with the antisolvent method. This is in contrast to a comparable $MAPbI_3$ study, which exhibits characteristic preferential crystal orientations after rapid thermal annealing (e.g. FIRA), but not when using the antisolvent method. (Figure 2e).

In contrast, the highly symmetric cubic crystal lattice of $MAPbBr_3$[38] yields isolated highly faceted domains that appear to consist of only a few individual single crystals (see Figure 1d-f). Hence, while the consistent $MAPbBr_3$ pattern morphology shows that the saturation threshold for nucleation at the Au seeds is lowered similarly to $MAPbI_3$, the growth rate has to be significantly higher to achieve completely isolated platelets under the same experimental conditions that yield complete substrate coverage by a $MAPbI_3$ film.

3 Conclusions

Using pre-patterned substrates, the nucleation of domains was controlled with Au seeds in FIRA-annealed perovskite films. The seeding lowers the nucleation threshold enabling an otherwise inaccessible regime in the kinetic space of nucleation and crystal growth. The modified nucleation site density and lowering of the nucleation threshold led to morphological differences that affect the micro-morphology of the polycrystalline perovskite films and their optoelectronic properties. It was shown that crystallite size in the domains correlates with crystal growth rate and solute concentration at the crystal growth front of growing domains. This result is important since it allows to engineer the crystallite size in nucleated perovskite films, allowing a systematic study of the electronic effects of grain boundaries, which in the long run will enable to improve the performance and lifetime of devices.

While Au seeds are a reliable nucleation catalyst and are easily patterned onto sub-

strates, they have the evident caveats in an optoelectronic device, introducing trap-states and recombination sites and contributing to faster degradation mechanisms. In the case where geometric patterning is not desired but seeding-assisted morphology control of compact films is the objective, other seeding particles as additives such as quantum dots are starting to be explored[55,56] and should be of interest especially in fabrication upscaling with single-step thermal annealing methods.

The spatial predetermination of the nucleation sites enables detailed local study of the nucleation and crystal growth processes as demonstrated in the *in-situ* experiments. Knowing the location of a nucleation site and the direction and scope of crystal growth a priori enables the locally targeted study of the evolution from precursor solution to perovskite crystal beyond the visual observation with the optical microscope.

Beyond PSCs, the deterministic patterning of isolated perovskite domains can be of interest for other applications of perovskite materials such as sensing, light-emission (e.g. LEDs and lasers), and light detection. Further optimising the seeding and annealing parameters with a device application in mind, obtaining large-scale perovskite arrays with near single crystal morphologies could be possible, similar to recent developments but compatible with the FIRA method.[57] This approach should also be compatible with thin film transfer methods such as template stripping, for example for applications requiring substrates that are incompatible with the growth of high quality perovskite films.[58]

4 Experimental Section

4.1 Substrate Patterning

A photoresist layer (ECI 3007, MicroChemicals) was spin-coated (Süss ACS200 Gen3) onto silicon or tin doped indium oxide (ITO) sputter coated (500 nm, Pfeiffer SPIDER 600) glass wafers. Hexagonal arrays of discs with 3 µm diameter and of varying pitches were exposed by a laser writer (405 nm, Heidelberg MLA150), and developed (AZ 726 MIF, MicroChemicals).

The wafers were then coated with a $1\,\text{nm}$ Cr and a $15\,\text{nm}$ Au layer by thermal evaporation (Minilab-80, Moorfield Nanotechnology), followed by a standard lift-off step (Remover 1165, Microposit), rinsing in IPA and H_2O, and a final blow dry with N_2. The wafers were then diced into $12 \times 12\,\text{mm}^2$ samples using a diamond scribe.

4.2   Perovskite Synthesis

The lead iodide (PbI_2) and lead bromide ($PbBr_2$) precursors were purchased from TCI, the organic salts methylammonium iodide (MAI), methylammonium bromide (MABr), formamidinium iodide (FAI) and formamidinium bromide (FABr) from Greatcell Solar Materials, and cesium iodide (CsI), anhydrous dimethylformamide (DMF) and anhydrous dimethylsulfoxide (DMSO) from Sigma-Aldrich.

The methylammonium lead tri-iodide ($MAPbI_3$) and methylammonium lead tri-bromide ($MAPbBr_3$) precursor solutions were prepared by mixing a 1:1 ratio of MAI and PbI_2 and MABr and $PbBr_2$ respectively in a 3:1 v/v DMF:DMSO solvent mixture or in pure DMF to obtain a concentration of $1.2\,\text{M}$. The triple cation ($Cs_{0.05}(MA_{0.17}FA_{0.83})_{0.95}Pb(I_{0.83}Br_{0.17})_3$) precursor solution was obtained from a 83:17 v:v ratio of 1.24M formamidinium lead tri-iodide ($FAPbI_3$) and $MAPbBr_3$ solutions, with an overstoichiometric ratio of 1:1.09 of both $MABr:PbBr_2$ and $FAI:PbI_2$, prepared in 4:1 v/v DMF:DMSO. For the $Cs_{0.15}FA_{0.85}PbI_3$ perovskite a $1.24\,\text{M}$ 1:1.09 over-stoichiometric $FAPbI_3$ solution was mixed with CsI in 4:1 v/v DMF:DMSO. The precursor solution preparation was carried out in a glove box under N_2 atmosphere.

The samples prepared with the flash infrared annealing (FIRA) method were prepared by spin-coating the precursor solution in a single step at $4000\,\text{rpm}$ for $10\,\text{s}$ onto patterned Si or ITO coated glass substrates (after $5\,\text{min}$ O_2 plasma etching), then irradiated for $1.4\,\text{s}$ in the FIRA chamber and kept inside the chamber for an additional $20\,\text{s}$. The entire process was carried out in a glove box under a N_2 atmosphere.

4.3 Microscopy and Structural Characterisation

For *in-situ* microscopy observations, the patterned silicon substrates were initially exposed to a 5 min O_2 plasma step and then kept at a constant elevated temperature on a Linkam HFS350X temperature controlled stage installed under a ZEISS Axio Scope.A1 optical microscope equipped with a Point Grey Grasshopper3 camera using a $20\times$ objective. Unless otherwise indicated, 2 µL of the respective precursor solution was drop-cast onto the heated substrate. The *in-situ* observations were limited to patterned Si substrates, since the Au patches on ITO coated glass substrates heat more strongly relative to the substrate than on Si, causing dewetting from these patches. In this case, perovskite nucleation occurs at the boundaries of the dewetted areas (Supplementary Information (SI) Figure S8).

X-ray diffraction (XRD) measurements on the films were performed using a Rigaku Ultima-IV diffractometer using Cu Kα radiation.

Scanning electron microscopy (SEM) images were obtained with a Tescan Mira3 LM FE SEM with a field emission source operated at an acceleration voltage of 5 kV using an Everhart-Thornley-type secondary electron detector.

For electron backscattering diffraction (EBSD) measurements, a direct-electron detector based on the Timepix sensor from Amsterdam Scientific Instruments (ASI) was used. The scanning parameters were 7 kV, 100 pA, 50 ms and 12.4 mm as voltage, current, exposure time and working distance, respectively. The used exposure time and the current correspond to the application of 5 nA ms electron dose per pixel. The step size of the measurement was 500 nm. EBSD data were collected using EDAX OIM software, and a Python script was used for image processing. The acquired Kikuchi patterns were indexed using tetragonal symmetry, I4/mcm, using 3° as the degree of tolerance. A detailed procedure for fitting the Hough's space is reported in Muscarella *et al.*[37]

The time resolved photoluminescence (TRPL) mapping system is based on PicoQuant systems composed by a FluoTime 300 unit and a microscope system (MicroTime 100). For excitation, a 639 nm laser with ~100 ps pulse width with a frequency of 3 MHz has been used.

The beam diameter was roughly $130\,\mu m$ (13.5% metric), as measured with a NanoScan2 beam profiler. The excitation photon density was $\sim 2 \times 1012\,\mathrm{photons/cm^2/pulse}$. To collect the emitted light, an Olympus long-range $20\times$ objective (LCPLN20XIR) with numerical aperture of 0.45 was used. The emitted light is guided to a detection fiber of $50\,\mu m$ acting as a pinhole, which is coupled to the FluoTime unit including the input optics to focus the light into the monochromator and the photomultiplier detector (PMA 192). A Time-Harp 260 Nano TCPSC card in long-range mode has been used for photon counting. A wide-range scanner stage from Physik Instrumente is used (M687.7) for mapping. The dwell time was set to $5\,\mathrm{ms/decay}$ with a step size $\sim 0.5\,\mu m/\mathrm{pixel}$. The system has a global illumination local detection configuration (widefield) with an optical resolution $\sim 2\,\mu m$. A single exponential equation has been used to fit the decay at each pixel. The samples used for TRPL correspond to a layer structure glass/ITO/local Au seeds/MAPbI$_3$.

Acknowledgement

Supporting Information Available

Additional SEM images: 50µm pitch MAPbBr$_3$, domain centers, platinum and copper nucleation seeds, final in-situ film; EBSD in-plane orientations; optical microscopy of in-situ crystallization of MA-free perovskite, XRD of triple cation FIRA and antisolvent, SEM image of MAPbBr$_3$, on Au-patterned ITO substrate, cross-section of patterned MAPbI$_3$, AFM image of patterned MAPbI$_3$.

References

(1) Green, M.; Dunlop, E.; Hohl-Ebinger, J.; Yoshita, M.; Kopidakis, N.; Hao, X. Solar Cell Efficiency Tables (Version 57). *Progress in Photovoltaics: Research and Applications* **2021**, *29*, 3–15.

(2) Jeon, N. J.; Noh, J. H.; Yang, W. S.; Kim, Y. C.; Ryu, S.; Seo, J.; Seok, S. I. Compositional Engineering of Perovskite Materials for High-Performance Solar Cells. *Nature* **2015**, *517*, 476–480.

(3) Saliba, M.; Matsui, T.; Seo, J. Y.; Domanski, K.; Correa-Baena, J. P.; Nazeeruddin, M. K.; Zakeeruddin, S. M.; Tress, W.; Abate, A.; Hagfeldt, A.; Grätzel, M. Cesium-Containing Triple Cation Perovskite Solar Cells: Improved Stability, Reproducibility and High Efficiency. *Energy and Environmental Science* **2016**, *9*, 1989–1997.

(4) National Renewable Energy Laboratory, Best Research-Cell Efficiency Chart. `https://www.nrel.gov/pv/assets/pdfs/best-research-cell-efficiencies.20200708.pdf`, accessed 01/2021.

(5) Pazos-Outón, L. M.; Xiao, T. P.; Yablonovitch, E. Fundamental Efficiency Limit of Lead Iodide Perovskite Solar Cells. *Journal of Physical Chemistry Letters* **2018**, *9*, 1703–1711.

(6) Shockley, W.; Queisser, H. J. Detailed Balance Limit of Efficiency of p-n Junction Solar Cells. *Journal of Applied Physics* **1961**, *32*, 510–519.

(7) Hu, H.; Singh, M.; Wan, X.; Tang, J.; Chu, C. W.; Li, G. Nucleation and Crystal Growth Control for Scalable Solution-Processed Organic-Inorganic Hybrid Perovskite Solar Cells. *Journal of Materials Chemistry A* **2020**, *8*, 1578–1603.

(8) Wang, F.; Cao, Y.; Chen, C.; Chen, Q.; Wu, X.; Li, X.; Qin, T.; Huang, W. Materials toward the Upscaling of Perovskite Solar Cells: Progress, Challenges, and Strategies. *Advanced Functional Materials* **2018**, *28*, 1803753.

(9) Murali, B.; Kolli, H. K.; Yin, J.; Ketavath, R.; Bakr, O. M.; Mohammed, O. F. Single Crystals: The Next Big Wave of Perovskite Optoelectronics. *ACS Materials Letters* **2020**, *2*, 184–214.

(10) Chen, Z.; Turedi, B.; Alsalloum, A. Y.; Yang, C.; Zheng, X.; Gereige, I.; Alsaggaf, A.; Mohammed, O. F.; Bakr, O. M. Single-Crystal MAPbI3 Perovskite Solar Cells Exceeding 21% Power Conversion Efficiency. *ACS Energy Letters* **2019**, *4*, 1258–1259.

(11) Lei, Y.; Chen, Y.; Zhang, R.; Li, Y.; Yan, Q.; Lee, S.; Yu, Y.; Tsai, H.; Choi, W.; Wang, K.; Luo, Y.; Gu, Y.; Zheng, X.; Wang, C.; Wang, C.; Hu, H.; Li, Y.; Qi, B.; Lin, M.; Zhang, Z.; Dayeh, S. A.; Pharr, M.; Fenning, D. P.; Lo, Y. H.; Luo, J.; Yang, K.; Yoo, J.; Nie, W.; Xu, S. A Fabrication Process for Flexible Single-crystal Perovskite Devices. *Nature* **2020**, *583*, 790–795.

(12) Lee, L.; Baek, J.; Park, K. S.; Lee, Y. E. K.; Shrestha, N. K.; Sung, M. M. Wafer-Scale Single-Crystal Perovskite Patterned Thin Films Based on Geometrically-Confined Lateral Crystal Growth. *Nature Communications* **2017**, *8*, 15882.

(13) Kayes, B. M.; Nie, H.; Twist, R.; Spruytte, S. G.; Reinhardt, F.; Kizilyalli, I. C.; Higashi, G. S. 27.6% Conversion efficiency, a New Record For Single-Junction Solar

Cells Under 1 Sun Illumination. *Conference Record of the IEEE Photovoltaic Specialists Conference* **2011**, 4–8.

(14) Metaferia, W.; Schulte, K. L.; Simon, J.; Johnston, S.; Ptak, A. J. Gallium Arsenide Solar Cells Grown at Rates Exceeding 300 µm h^{-1} by Hydride Vapor Phase Epitaxy. *Nature Communications* **2019**, *10*, 3361.

(15) Tailor, N. K.; Abdi-Jalebi, M.; Gupta, V.; Hu, H.; Dar, M. I.; Li, G.; Satapathi, S. Recent Progress in Morphology Optimization in Perovskite Solar Cell. *Journal of Materials Chemistry A* **2020**, *8*, 21356–21386.

(16) Li, Y.; Ji, L.; Liu, R.; Zhang, C.; Mak, C. H.; Zou, X.; Shen, H. H.; Leu, S. Y.; Hsu, H. Y. A Review on Morphology Engineering for Highly Efficient and Stable Hybrid Perovskite Solar Cells. *Journal of Materials Chemistry A* **2018**, *6*, 12842–12875.

(17) Zhang, W.; Saliba, M.; Moore, D. T.; Pathak, S. K.; Hörantner, M. T.; Stergiopoulos, T.; Stranks, S. D.; Eperon, G. E.; Alexander-Webber, J. A.; Abate, A.; Sadhanala, A.; Yao, S.; Chen, Y.; Friend, R. H.; Estroff, L. A.; Wiesner, U.; Snaith, H. J. Ultrasmooth Organic-Inorganic Perovskite Thin-Film Formation and Crystallization for Efficient Planar Heterojunction Solar Cells. *Nature Communications* **2015**, *6*, 6142.

(18) Steirer, K. X.; Schulz, P.; Teeter, G.; Stevanovic, V.; Yang, M.; Zhu, K.; Berry, J. J. Defect Tolerance in Methylammonium Lead Triiodide Perovskite. *ACS Energy Letters* **2016**, *1*, 360–366.

(19) Lee, J. W.; Bae, S. H.; De Marco, N.; Hsieh, Y. T.; Dai, Z.; Yang, Y. The Role of Grain Boundaries in Perovskite Solar Cells. *Materials Today Energy* **2018**, *7*, 149–160.

(20) Foley, B. J.; Girard, J.; Sorenson, B. A.; Chen, A. Z.; Scott Niezgoda, J.; Alpert, M. R.; Harper, A. F.; Smilgies, D. M.; Clancy, P.; Saidi, W. A.; Choi, J. J. Controlling Nucleation, Growth, and Orientation of Metal Halide Perovskite Thin Films with Rationally Selected Additives. *Journal of Materials Chemistry A* **2017**, *5*, 113–123.

(21) Pham, N. D.; Tiong, V. T.; Yao, D.; Martens, W.; Guerrero, A.; Bisquert, J.; Wang, H. Guanidinium Thiocyanate Selective Ostwald Ripening Induced Large Grain for High Performance Perovskite Solar Cells. *Nano Energy* **2017**, *41*, 476–487.

(22) Bae, S.; Jo, J. W.; Lee, P.; Ko, M. J. Controlling the Morphology of Organic-Inorganic Hybrid Perovskites through Dual Additive-Mediated Crystallization for Solar Cell Applications. *ACS Applied Materials and Interfaces* **2019**, *11*, 17452–17458.

(23) Wang, F.; Shimazaki, A.; Yang, F.; Kanahashi, K.; Matsuki, K.; Miyauchi, Y.; Takenobu, T.; Wakamiya, A.; Murata, Y.; Matsuda, K. Highly Efficient and Stable Perovskite Solar Cells by Interfacial Engineering Using Solution-Processed Polymer Layer. *Journal of Physical Chemistry C* **2017**, *121*, 1562–1568.

(24) Roose, B.; Dey, K.; Chiang, Y.-H.; Friend, R. H.; Stranks, S. D. A Critical Assessment of the Use of Excess Lead Iodide in Lead Halide Perovskite Solar Cells. *The Journal of Physical Chemistry Letters* **2020**, *11*, 6505–6512.

(25) Fu, Y.; Zhu, H.; Chen, J.; Hautzinger, M. P.; Zhu, X. Y.; Jin, S. Metal Halide Perovskite Nanostructures for Optoelectronic Applications and the Study of Physical Properties. *Nature Reviews Materials* **2019**, *4*, 169–188.

(26) Watson, B. L.; Rolston, N.; Printz, A. D.; Dauskardt, R. H. Scaffold-Reinforced Perovskite Compound Solar Cells. *Energy Environ. Sci.* **2017**, *10*, 2500–2508.

(27) Yang, X.; Wu, J.; Liu, T.; Zhu, R. Patterned Perovskites for Optoelectronic Applications. *Small Methods* **2018**, *2*, 1800110.

(28) Sanchez, S.; Hua, X.; Phung, N.; Steiner, U.; Abate, A. Flash Infrared Annealing for Antisolvent-Free Highly Efficient Perovskite Solar Cells. *Advanced Energy Materials* **2018**, *8*, 1702915.

(29) Sánchez, S.; Vallés-Pelarda, M.; Alberola-Borràs, J. A.; Vidal, R.; Jerónimo-Rendón, J. J.; Saliba, M.; Boix, P. P.; Mora-Seró, I. Flash Infrared Annealing as a Cost-Effective and Low Environmental Impact Processing Method for Planar Perovskite Solar Cells. *Materials Today* **2019**, *31*, 39–46.

(30) He, M.; Li, B.; Cui, X.; Jiang, B.; He, Y.; Chen, Y.; O'Neil, D.; Szymanski, P.; El-Sayed, M. A.; Huang, J.; Lin, Z. Meniscus-Assisted Solution Printing of Large-Grained Perovskite Films for High-Efficiency Solar Cells. *Nature Communications* **2017**, *8*, 16045.

(31) Sanchez, S.; Steiner, U.; Hua, X. Phase Evolution during Perovskite Formation - Insight from Pair Distribution Function Analysis. *Chemistry of Materials* **2019**, *31*, 3498–3506.

(32) Sánchez, S.; Hua, X.; Günzler, A.; Bermúdez-Ureña, E.; Septiadi, D.; Saliba, M.; Steiner, U. Flash Infrared Pulse Time Control of Perovskite Crystal Nucleation and Growth from Solution. *Crystal Growth and Design* **2020**, *20*, 670–679.

(33) Geske, T.; Li, J.; Worden, M.; Shan, X.; Chen, M.; Bade, S. G. R.; Yu, Z. Deterministic Nucleation for Halide Perovskite Thin Films with Large and Uniform Grains. *Advanced Functional Materials* **2017**, *27*, 1702180.

(34) Li, Y.; Zhi, L.; Ge, G.; Zhao, Z.; Cao, X.; Chen, F.; Cui, X.; Lin, F.; Ci, L.; Sun, J.; Zhuang, D.; Wei, J. Investigation on Crystallization of $CH_3NH_3PbI_3$ Perovskite and its Intermediate Phase from Polar Aprotic Solvents. *Crystal Growth and Design* **2019**, *19*, 959–965.

(35) Ash, P. F.; Bolker, E. D. Generalized Dirichlet Tessellations. *Geometriae Dedicata* **1986**, *20*, 209–243.

(36) Dunlap-Shohl, W. A.; Zhou, Y.; Padture, N. P.; Mitzi, D. B. Synthetic Approaches for Halide Perovskite Thin Films. *Chemical Reviews* **2019**, *119*, 3193–3295.

(37) Muscarella, L. A.; Hutter, E. M.; Sanchez, S.; Dieleman, C. D.; Savenije, T. J.; Hagfeldt, A.; Saliba, M.; Ehrler, B. Crystal Orientation and Grain Size: Do They Determine Optoelectronic Properties of MAPbI$_3$ Perovskite? *Journal of Physical Chemistry Letters* **2019**, *10*, 6010–6018.

(38) Chen, F.; Zhu, C.; Xu, C.; Fan, P.; Qin, F.; Gowri Manohari, A.; Lu, J.; Shi, Z.; Xu, Q.; Pan, A. Crystal Structure and Electron Transition Underlying Photoluminescence of Methylammonium Lead Bromide Perovskites. *Journal of Materials Chemistry C* **2017**, *5*, 7739–7745.

(39) Lamer, V. K.; Dinegar, R. H. Theory, Production and Mechanism of Formation of Monodispersed Hydrosols. *Journal of the American Chemical Society* **1950**, *72*, 4847–4854.

(40) Ding, B.; Li, Y.; Huang, S. Y.; Chu, Q. Q.; Li, C. X.; Li, C. J.; Yang, G. J. Material Nucleation/Growth Competition Tuning towards Highly Reproducible Planar Perovskite Solar Cells with Efficiency Exceeding 20%. *Journal of Materials Chemistry A* **2017**, *5*, 6840–6848.

(41) Cho, N.; Li, F.; Turedi, B.; Sinatra, L.; Sarmah, S. P.; Parida, M. R.; Saidaminov, M. I.; Murali, B.; Burlakov, V. M.; Goriely, A.; Mohammed, O. F.; Wu, T.; Bakr, O. M. Pure Crystal Orientation and Anisotropic Charge Transport in Large-Area Hybrid Perovskite Films. *Nature Communications* **2016**, *7*, 13407.

(42) Hasan, M. M.; Clegg, C.; Manning, M.; El Ghanam, A.; Su, C.; Harding, M. D.; Bennett, C.; Hill, I. G.; Koleilat, G. I. Stable Efficient Methylammonium Lead Iodide Thin Film Photodetectors with Highly Oriented Millimeter-Sized Crystal Grains. *ACS Photonics* **2020**, *7*, 57–67.

(43) D'Innocenzo, V.; Srimath Kandada, A. R.; De Bastiani, M.; Gandini, M.; Petrozza, A.

Tuning the Light Emission Properties by Band Gap Engineering in Hybrid Lead Halide Perovskite. *Journal of the American Chemical Society* **2014**, *136*, 17730–17733.

(44) Domanski, K.; Correa-Baena, J.-P.; Mine, N.; Nazeeruddin, M. K.; Abate, A.; Saliba, M.; Tress, W.; Hagfeldt, A.; Grätzel, M. Not All That Glitters Is Gold: Metal-Migration-Induced Degradation in Perovskite Solar Cells. *ACS Nano* **2016**, *10*, 6306–6314.

(45) Wei, D.; Wang, T.; Ji, J.; Li, M.; Cui, P.; Li, Y.; Li, G.; Mbengue, J. M.; Song, D. Photo-Induced Degradation of Lead Halide Perovskite Solar Cells Caused by the Hole Transport Layer/Metal Electrode Interface. *Journal of Materials Chemistry A* **2016**, *4*, 1991–1998.

(46) Jeong, B.; Han, H.; Park, C. Micro- and Nanopatterning of Halide Perovskites where Crystal Engineering for Emerging Photoelectronics Meets Integrated Device Array Technology. *Advanced Materials* **2020**, *32*, 2000597.

(47) Deng, Y.; Wang, Q.; Yuan, Y.; Huang, J. Vividly Colorful Hybrid Perovskite Solar Cells by Doctor-Blade Coating with Perovskite Photonic Nanostructures. *Materials Horizons* **2015**, *2*, 578–583.

(48) Hu, Q.; Zhao, L.; Wu, J.; Gao, K.; Luo, D.; Jiang, Y.; Zhang, Z.; Zhu, C.; Schaible, E.; Hexemer, A.; Wang, C.; Liu, Y.; Zhang, W.; Grätzel, M.; Liu, F.; Russell, T. P.; Zhu, R.; Gong, Q. *In situ* Dynamic Observations of Perovskite Crystallisation and Microstructure Evolution Intermediated from $[PbI_6]^{4-}$ Cage Nanoparticles. *Nature Communications* **2017**, *8*, 15688.

(49) Bangsund, J. S.; Fielitz, T. R.; Steiner, T. J.; Shi, K.; Van Sambeek, J. R.; Clark, C. P.; Holmes, R. J. Formation of Aligned Periodic Patterns during the Crystallization of Organic Semiconductor Thin Films. *Nature Materials* **2019**, *18*, 725–731.

(50) Wu, Y.; Islam, A.; Yang, X.; Qin, C.; Liu, J.; Zhang, K.; Peng, W.; Han, L. Retarding the Crystallization of PbI2 for Highly Reproducible Planar-Structured Perovskite Solar Cells via Sequential Deposition. *Energy and Environmental Science* **2014**, *7*, 2934–2938.

(51) Miyamae, H.; Numahata, Y.; Nagata, M. The Crystal Structure Of Lead(II)Iodide-Dimethylsulphoxide(1/2), $PbI_2(DMSO)_2$. *Chemistry Letters* **1980**, *9*, 663–664.

(52) Cao, X.; Zhi, L.; Jia, Y.; Li, Y.; Zhao, K.; Cui, X.; Ci, L.; Zhuang, D.; Wei, J. A Review of the Role of Solvents in Formation of High-Quality Solution-Processed Perovskite Films. *ACS Applied Materials and Interfaces* **2019**, *11*, 7639–7654.

(53) Bercegol, A.; Ramos, F. J.; Rebai, A.; Guillemot, T.; Puel, J. B.; Guillemoles, J. F.; Ory, D.; Rousset, J.; Lombez, L. Spatial Inhomogeneity Analysis of Cesium-Rich Wrinkles in Triple-Cation Perovskite. *Journal of Physical Chemistry C* **2018**, *122*, 23345–23351.

(54) Zheng, G.; Zhu, C.; Ma, J.; Zhang, X.; Tang, G.; Li, R.; Chen, Y.; Li, L.; Hu, J.; Hong, J.; Chen, Q.; Gao, X.; Zhou, H. Manipulation of Facet Orientation in Hybrid Perovskite Polycrystalline Films by Cation Cascade. *Nature Communications* **2018**, *9*, 2793.

(55) Lin, C. Y.; Li, S. S.; Chang, J. W.; Chia, H. C.; Hsiao, Y. Y.; Su, C. J.; Lian, B. J.; Wen, C. Y.; Huang, S. K.; Wu, W. R.; Wang, D. Y.; Su, A. C.; Chen, C. W.; Jeng, U. S. Unveiling the Nanoparticle-Seeded Catalytic Nucleation Kinetics of Perovskite Solar Cells by Time-Resolved GIXS. *Advanced Functional Materials* **2019**, *29*, 1902582.

(56) Liu, M.; Chen, Y.; Tan, C. S.; Quintero-Bermudez, R.; Proppe, A. H.; Munir, R.; Tan, H.; Voznyy, O.; Scheffel, B.; Walters, G.; Kam, A. P. T.; Sun, B.; Choi, M. J.; Hoogland, S.; Amassian, A.; Kelley, S. O.; García de Arquer, F. P.; Sargent, E. H. Lattice Anchoring Stabilizes Solution-Processed Semiconductors. *Nature* **2019**, *570*, 96–101.

(57) Lei, Y.; Chen, Y.; Zhang, R.; Li, Y.; Yan, Q.; Lee, S.; Yu, Y.; Tsai, H.; Choi, W.; Wang, K.; Luo, Y.; Gu, Y.; Zheng, X.; Wang, C.; Wang, C.; Hu, H.; Li, Y.; Qi, B.; Lin, M.; Zhang, Z.; Dayeh, S. A.; Pharr, M.; Fenning, D. P.; Lo, Y.-H.; Luo, J.; Yang, K.; Yoo, J.; Nie, W.; Xu, S. A Fabrication Process for Flexible Single-Crystal Perovskite Devices. *Nature* **2020**, *583*, 790–795.

(58) Hernandez Oendra, A. C.; De Leo, E.; Koepfli, S. M.; Winkler, J. M.; Rossinelli, A. A.; Riedinger, A.; Norris, D. J.; Prins, F. Template Stripping of Perovskite Thin Films for Dry Interfacing and Surface Structuring. *ACS Applied Materials & Interfaces* **2020**, *12*, 26601–26606.